Room temperature electron spin coherence in telecom-wavelength quaternary quantum wells

W. H. Lau, V. Sih, N. P. Stern, R. C. Myers, D. A. Buell, A. C. Gossard, and D. D. Awschalom*

Center for Spintronics and Quantum Computation,
University of California, Santa Barbara, CA 93106
(Dated: February 6, 2008)

Time-resolved Kerr rotation spectroscopy is used to monitor the room temperature electron spin dynamics of optical telecommunication wavelength AlInGaAs multiple quantum wells lattice-matched to InP. We found that electron spin coherence times and effective g-factors vary as a function of aluminum concentration. The measured electron spin coherence times of these multiple quantum wells, with wavelengths ranging from 1.26 μm to 1.53 μm, reach approximately 100 ps at room temperature, and the measured electron effective g-factors are in the range from -2.3 to -1.1.

Recent developments in semiconductor-based spintronics and quantum computation[1,2] have generated intense interest in examining the spin dynamics in a wide range of semiconductor material systems at telecom wavelengths[3,4,5,6] due to their potential applications in spin-dependent optical modulators and switches for optical telecommunications[6,7,8,9]. The optical wavelengths of 1.31 μm and 1.55 μm allow a minimum dispersion and signal loss in standard silica-based fiber-optic networks. Spin-dependent all-optical switching in semiconductor quantum well etalons[8] and spin-dependent ultrafast optical gain modulation in microcavity lasers have been recently demonstrated[9]. In addition, differential quantum efficiency as high as 64% is attainable for all-epitaxially grown telecom-wavelength vertical cavity surface emitting lasers (VCSELs) with InP lattice-matched AlInGaAs alloys for quantum well active regions and AlGaAsSb alloys for highly reflective distributed Bragg reflectors operating above room temperature[10,11]. The possibility of integrating laser sources, optical modulators, and optical switches on a single photonic integrated chip with added functionalities based on spin degrees of freedom makes AlInGaAs alloys ideal candidates for spintronics.

In this letter, we present room temperature measurements of the electron spin coherence times and effective g-factors in AlInGaAs multiple quantum wells, which are optimized active regions of VCSELs with wavelengths in the range $1.26 - 1.53$ μm designed for optical telecommunication applications[10,11]. We characterize the samples using photoluminescence and measure the electron spin dynamics using pump-probe optical spectroscopy. The electron effective g-factors and spin coherence times are found to vary with aluminum alloy concentration from -2.3 to -1.1 and from 50 ps to 100 ps, respectively.

Our samples are comprised of a set of quaternary alloy AlInGaAs multiple quantum wells grown using digital alloy molecular beam epitaxy. These samples are composed of digital alloys of ternaries ($Ga_{0.47}In_{0.53}As$ and $Al_{0.48}In_{0.52}As$, referred to as GaInAs and AlInAs, respectively) lattice-matched to InP[10]. The sample structure is of the form: $AlInAs/(AlIn)_r(GaIn)_{1-r}As/5x[(AlIn)_y(GaIn)_{1-y}As$
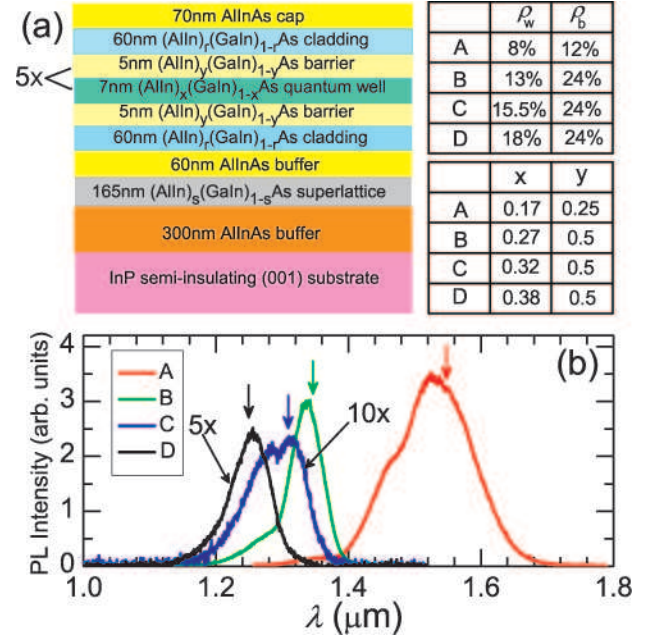

FIG. 1: (Color) (a) Sample structure of multiple quantum wells, where $r = 0.75$ and $s = 0.82$, and 5x signifies the growth repetition. The average aluminum concentration of the quantum wells and barriers are ρ_w and ρ_b, respectively. (b) Photoluminescence spectra at room temperature. The vertical arrows indicate the positions of the calculated effective band gaps. The intensity of the PL spectra for Sample C and Sample D is scaled for clarity.

$/(AlIn)_x(GaIn)_{1-x}As]/(AlIn)_y(GaIn)_{1-y}As/(AlIn)_r$ $(GaIn)_{1-r}As/AlInAs/(AlIn)_s(GaIn)_{1-s}As/AlInAs/InP$ substrate, shown schematically in Fig.1(a). All samples are undoped. The photoluminescence (PL) spectra of these samples are excited non-resonantly with 2.5 mW of 800 nm light from a tunable mode-locked Ti:sapphire laser and measured using a liquid nitrogen cooled InGaAs photodiode array detector [Fig. 1(b)]. The PL peaks of the samples at room temperature occur at 1.53 μm (Sample A), 1.34 μm (Sample B), 1.30 μm (Sample C), and 1.26 μm (Sample D), and the corresponding energies are 0.811 eV, 0.925 eV, 0.954 eV,
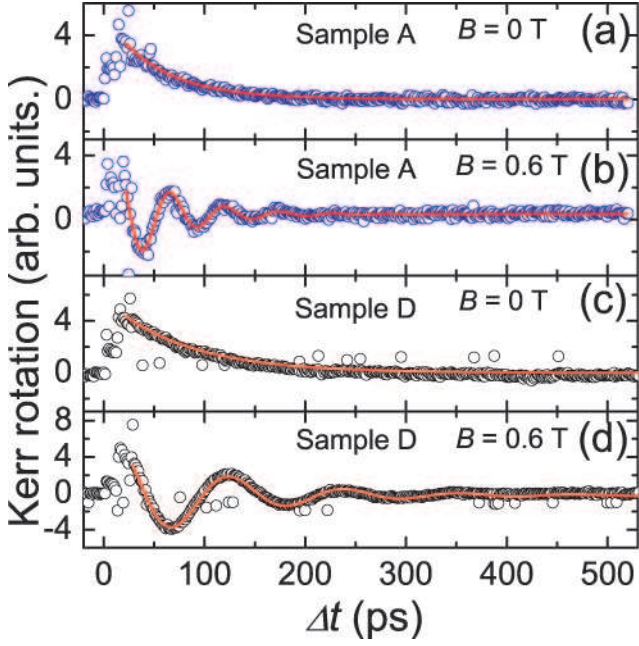
FIG. 2: (Color) Time-resolved Kerr rotation of Sample A at room temperature for (a) $B = 0$ T, and (b) $B = 0.6$ T, and Sample D for (c) $B = 0$ T, and (d) $B = 0.6$ T. Offset is subtracted for clarity. Circles are measurements and lines are fits using the expression for $\theta(\Delta t)$.

FIG. 3: (Color) (a) Electron spin coherence time T_2^*, and (b) spin precession frequency ν_L as a function of magnetic field B at room temperature. The corresponding lines are linear fits.

and 0.984 eV, respectively. The PL intensity decreases with increasing aluminum concentration ρ_w due to Al incorporated impurities, such as oxygen, and lower confinement of the electron wave functions arising from lower conduction band offsets. The PL spectrum of Sample C consists of two broad peaks (1.28 μm and 1.30 μm), and the 1.28 μm peak might be due to impurity broadening. We calculate the effective band gaps of the quantum wells using a generalized fourteen-band $\mathbf{K} \cdot \mathbf{p}$ envelope-function theory[12,13], and the calculated effective band gaps for Samples A-D are 1.55 μm, 1.35 μm, 1.30 μm, and 1.25 μm, respectively.

Time-resolved Kerr rotation (TRKR), an optical pump-probe spectroscopic technique[14], is used to probe the electron spin dynamics. An optical parametric amplifier pumped by a regeneratively amplified Ti:sapphire mode-locked laser produces $\sim$ 200 fs duration pump and probe pulses tunable from 1.1 μm to 1.65 μm with a repetition rate of 100 kHz, whose relative delay is adjusted by a mechanical delay line. The helicity of the pump beam for spin injection is modulated with a photoelastic modulator at 42 kHz, and the linearly polarized probe beam for spin detection is mechanically chopped at a frequency of 800 Hz. The pump and probe beams are focused to a spot size of $\sim 50 \mu$m on the sample, which is mounted between the two poles of an electro-magnet which provides a magnetic field B up to 0.6 T and perpendicular to the direction of the pump and probe beams. The circularly polarized pump beam excites electron and hole spins which precess at 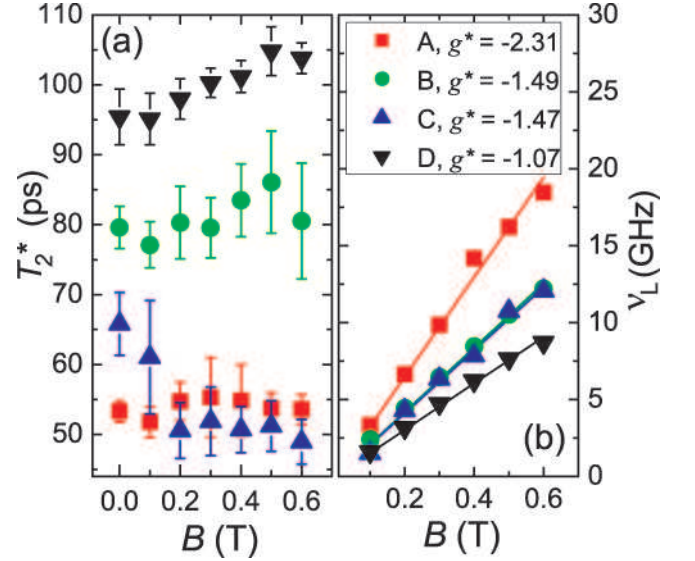the Larmor frequency around the transverse applied magnetic field. The typical pump and probe powers used in the measurements are 1 mW and 0.1 mW, respectively. The rotation of the linear polarization axis of the probe beam is proportional to the net electron spin polarization along the probe's normal incidence. Using a balanced photodiode bridge combined with a lock-in detection technique, the electron spin precession is measured with subpicosecond temporal resolution[14].

In Fig. 2, we show representative TRKR scans for Sample A (8% Al) and Sample D (18% Al) at room temperature with applied magnetic fields $B = 0$ T and $B = 0.6$ T. The electron spin magnetization precesses in the plane perpendicular to the applied magnetic field, and the Kerr rotation angle as a function of time delay Δt can be described by an exponentially decaying cosine: $\theta(\Delta t) = \theta_o \exp(-t/T_2^*) \cos(2\pi \nu_L \Delta t)$, where θ_o is the initial amplitude of the electron spin polarization, ν_L is the Larmor precession frequency $\nu_L = g^* \mu_B B/h$, where g^* is the effective in-plane electron g-factor of electrons in the quantum wells, μ_B is the Bohr magneton, h is Planck's constant, and T_2^* is the electron spin coherence time. The data are fit by adjusting the parameters θ_o, T_2^*, and g^*. The lack of additional frequency components and the agreement of g^* with the expected value[15,16] for electrons indicate that hole spin precession is not observable.

The magnetic field dependence of T_2^* at room temperature for all four samples is plotted in Fig. 3(a). All the samples exhibit weak magnetic field dependence. The corresponding Larmor frequencies ν_L of all samples have a linear magnetic field dependence [Fig. 3(b)], yielding $|g^*| = 2.31$ (Sample A), $|g^*| = 1.49$ (Sample B), $|g^*| = 1.47$ (Sample C), and $|g^*| = 1.07$ (Sample D). Although
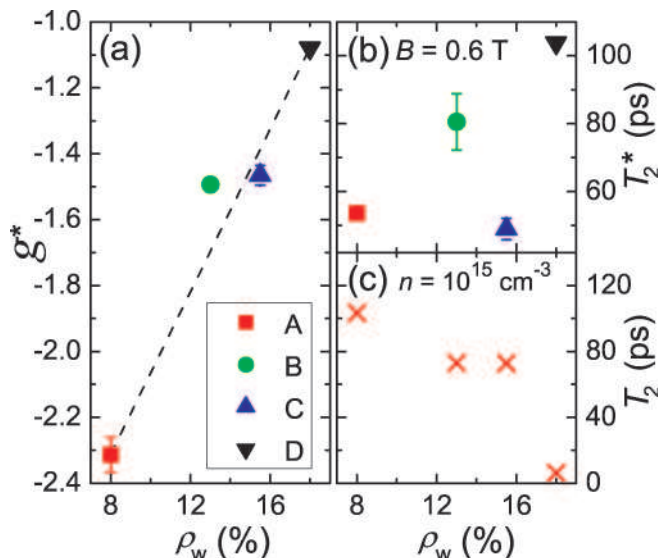
FIG. 4: (Color) Electron effective g-factor g^* (a), electron spin coherence time T_2^* for $B = 0.6$ T (b), and calculated T_2 (c) as a function of ρ_w. Red crosses represent the calculated T_2 assuming $\mu = 2000$ cm^2/Vs. n is electron density used in the calculations. Line is guide to the eyes.

the sign of g^* cannot be determined from our measurements, the fact that bulk InAs has a large and negative g-factor, while bulk AlAs has a small positive g-factor indicates that g^* is negative[15,16]. The electron effective g-factor as a function of ρ_w at room temperature is plotted in Fig. 4(a), showing g^* increases with increasing ρ_w consistent with the expected trends[15,16].

The electron spin coherence time T_2^* as a function of ρ_w at room temperature with applied magnetic field $B = 0.6$ T is displayed in Fig. 4(b). The measured electron spin coherence times are in the range from 50 ps to 100 ps. T_2^* increases with increasing ρ_w except for Sample C. The observed nonlinear ρ_w dependence of T_2^* is due to the combined effects of orbital scattering and internal effective magnetic field in the quantum wells[12,13].

Electron spin relaxation near room temperature is dominated by the D'yakonov-Perel' mechanism[13,17], and the spin relaxation rate is $T_2^{-1} \propto \Omega^2 \tau_\mathrm{o}$, where Ω is the momentum-dependent precession frequency about the internal effective magnetic field of the quantum wells and τ_o is the orbital coherence time, which is proportional to the electron mobility μ. As ρ_w increases, Ω increases due to band structure effects on the effective internal magnetic field, causing T_2 to decrease with increasing ρ_w. To illustrate these effects, we calculate the spin coherence times T_2 as a function of ρ_w for Samples A-D assuming a constant mobility for all samples using a generalized 14-band $\mathbf{K} \cdot \mathbf{p}$ envelope-function theory[12,13,18], and the results are shown in Fig. 4(c). However, the observed trends in T_2^* might be partly due to the nonlinear ρ_w dependence of the electron mobility in these samples. As ρ_w increase, τ_o decreases due to orbital scattering, causing T_2 to increase with increasing ρ_w. Finally, imperfection in crystal growth may lead to structural inversion asymmetry in the quantum wells, which generates an additional internal effective magnetic field contributing to electron spin decoherence[12].

We have measured the electron spin coherence times and electron spin precession frequencies in telecom-wavelength quaternary multiple quantum wells and observed the electron spin coherence times of $\sim$ 100 ps at room temperature. Our measurements reveal that the electron effective g-factor can be tuned by varying the aluminum alloy concentration. These results demonstrate the possibility of optical modulation using spin manipulation in this material system.

* Electronic address: awsch@physics.ucsb.edu

1 S. A. Wolf, D. D. Awschalom, R. A. Buhrman, J. M. Daughton, S. von Molnar, M. L. Roukes, A. Y. Chtchelkanova and D. M. Treger, Science **294**, 1488 (2001).

2 Semiconductor Spintronics and Quantum Computation, edited by D. D. Awschalom, D. Loss, and N. Samarth, Springer-Verlag, Berlin,(2002).

3 A. Tackeuchi, O. Wada, and Y. Nishikawa, Appl. Phys. Lett. **70**, 1131 (1997).

4 K. C. Hall, S. W. Leonard, H. M. van Driel, A. R. Kost, E. Selvig, and D. H. Chow, Appl. Phys. Lett. **75**, 4156 (1999).

5 S. Akasaka, S. Miyata, T. Kuroda, and A. Tackeuchi, Appl. Phys. Lett. **85**, 2083 (2004).

6 D. Marshall, M. Mazilu, A. Miller, and C. C. Button, J. Appl. Phys. **91**, 4049 (2002).

7 A. Tackeuchi, S. Muto, T. Inata, and T. Fugii, Appl. Phys. Lett. **56**, 2213 (1990).

8 Y. Nishikawa, A. Tackeuchi, S. Nakamura, S. Muto, and N. Yokoyama, Appl. Phys. Lett. **66**, 839 (1995).

9 M. Oestreich, S. Hallstein, and W. W. Ruhle, IEEE, J. Select. Topics Quantum Electron., **2**, 747 (1996).

10 D. A. Buell, D. Feezell, B. O. Finland, and L. A. Coldren, J. Vac. Sci. Technol., B **24**, 1544 (2006).

11 D. Feezell, D. A. Buell, and L. A. Coldren, IEEE Photon. Technol. Lett., **17**, 2017 (2005).

12 W. H. Lau and M. E. Flatté, Phys. Rev. B **72**, 161311(R) (2005).

13 W. H. Lau, J. T. Olesberg, and M. E. Flatté, cond-mat/0406201.

14 S. A. Crooker, D. D. Awschalom, J. J. Baumberg, F. Flack, and N. Samarth, Phys. Rev. B **56**, 7574 (1997).

15 Y. Lin, J. Nitta, T. Koga, and T. Akazaki, Physica E **21**, 656 (2004).

16 O. Madelung, Semiconductors: Data Handbook (Spinger, Berlin, 2003).

17 M. I. D'yakanov and V. I. Perel', Zh. Ekxp. Teor. Fiz. **60**,

1954 (1971)[Sov. Phys. JETP **42** , 1053 (1971)].

[18] Band structure parameters used in the calculations can be

found in Ref. 13.